Check for updates

How do bubbles affect light absorption in photoelectrodes for solar water splitting?

Abhinav Bhanawat, [ID] [a] Keyong Zhu[b] and Laurent Pilon [ID] *[a]

This paper aims to systematically investigate the effect of gas bubble formation on the performance of a horizontal photoelectrode exposed to normally incident light during photoelectrochemical water splitting. The presence of hydrogen or oxygen gas bubbles increases the back-scattering losses from the photoelectrode, thereby decreasing the photocurrent density generated. To quantify these optical losses, the normal-hemispherical reflectance of a Si photoelectrode covered with non-absorbing cap-shaped gas bubbles was predicted using the Monte Carlo ray-tracing method. For the first time, results are reported for both monodisperse and polydisperse bubbles with diameter ranging between 0.25 and 1.75 mm, projected surface area coverage varying between 0 and 78.5%, and contact angle ranging between 0° and 180°. The normal-hemispherical reflectance of the photoelectrode was found to be independent of the bubble diameter, and spatial and size distribution for any given projected surface area coverage. However, it varied significantly with the bubble contact angle due to total internal reflection at the electrolyte/bubble interface. The normal-hemispherical reflectance also increased with increasing projected surface area coverage thereby reducing the photon flux absorbed in the photoelectrode. In fact, the photons were absorbed mostly outside the bubble projection where they were preferentially scattered by the bubbles. The area-averaged absorptance in a bubble-covered Si photoelectrode reduced by up to 18% compared with a bare photoelectrode. The results presented in this study indicate that the performance of large photoelectrodes can be improved by using hydrophilic photoelectrodes or coatings.

1. Introduction

Photoelectrochemistry is one of the most promising technologies to drive redox reactions using solar radiation.[1] Upon absorbing photons from sunlight, photoactive semiconductors generate electron–hole pairs that can directly participate in redox reactions. One of the most common applications of photoelectrochemistry consists of generating hydrogen (H_2) gas *via* photoelectrochemical water splitting. This technology has gained significant attention in recent years in light of depleting fossil fuels and in the quest for cleaner alternative fuels and energy carriers to reduce greenhouse gas emissions and to mitigate global climate change.[2,3]

Photoelectrochemical water splitting is usually achieved by three pathways: photocatalysis (PC), photoelectrochemical cell (PEC cell), and photovoltaic-driven electrocatalysis (PV-EC).[4] Among these three technologies, PEC cell technology has been identified as the most scalable and economically viable for producing substantial amounts of H_2 gas for commercial applications.[4–6] In fact, the US Department of Energy has set the ultimate target of achieving 25% solar-to-hydrogen (STH) efficiency using concentrated illumination to bring down the cost of H_2 gas generated using PEC cell technology.[7] Such high efficiency requires generating a high photocurrent density in the PEC cell.

A typical PEC cell for solar water splitting consists of a photoelectrode, a counter electrode, and a reference electrode in a three-electrode configuration, all immersed in an aqueous electrolyte.[8,9] The photoelectrode is exposed to a flux of photons with energy larger than the band gap of the semiconductor photoelectrode material. Absorption of these photons results in redox reactions at the photoelectrode/electrolyte interface and in the release of gaseous products. The photoelectrode is usually made of PV grade materials such as Si and GaAs, or metal oxides including TiO_2 and $BiVO_4$, and may be used as either anode or cathode.[4] When used as a cathode, H_2 gas is released at its surface, while O_2 gas is released at the anode unexposed to light. These gases are released in the form of bubbles at nucleation sites on the surface of the electrodes.[10] The gas bubbles usually remain attached to the electrode surface until they grow sufficiently large for buoyancy to overcome surface tension forces. Then, bubbles detach, rise through the electrolyte, and burst at the electrolyte free surface. Fig. 1 presents photographs of typical

[a]Mechanical and Aerospace Engineering Department, University of California, Los Angeles, CA, USA. E-mail: pilon@seas.ucla.edu

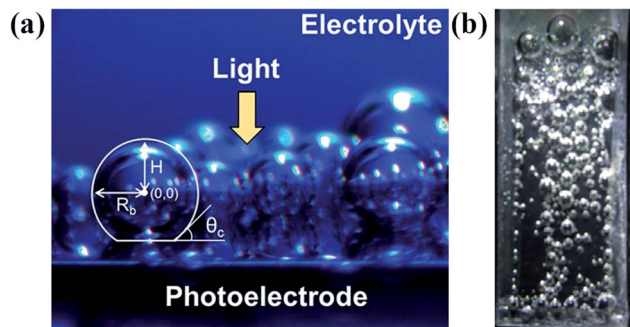[b]Beihang University School of Aeronautic Science and Engineering, Beijing, China

Fig. 1 (a) Hydrogen gas bubbles obstructing the incident light on a horizontal Si photoelectrode immersed in an aqueous electrolyte (reprinted with permission from ref. 11. Copyright © 2017 American Chemical Society). (b) Hydrogen gas bubbles generated on a vertical Pt photoelectrode immersed in an aqueous electrolyte (reprinted from ref. 12, Copyright © 2019 with permission from Elsevier).

bubble-covered Si or Pt photocathodes in (a) horizontal[11] or (b) vertical orientations[12] showing significant fraction of the photoelectrode area covered with bubbles. Fig. 1(a) also indicates that the bubbles are approximately spherical cap-shaped for horizontal orientation.

The bubbles present on the surface of a gas-evolving electrode can lead to kinetic and ohmic losses, which have been extensively studied.[13–15] In brief, the presence of bubbles on the photoelectrode surface reduces the electrochemically active surface area and increases the kinetic overpotential necessary to drive the redox reactions.[10,16] The bubbles also present additional resistance to the flow of current between the electrodes through the electrolyte, thereby increasing the ohmic overpotential for the reaction.[10]

In photoelectrochemistry, the presence of bubbles is also responsible for optical losses. Indeed, the generated gas bubbles reduce the photon flux reaching the photoelectrode.[17,18] The curvature of bubbles and the refractive index mismatch at the electrolyte/bubble interface can lead to reflection, refraction, and total internal reflection causing back-scattering of incident photons and significant redistribution of the incident light intensity on the photoelectrode surface.[11,12] These optical effects reduce the photocurrent density generated in the photoelectrode, and ultimately, the efficiency of a photoelectrochemical (PEC) cell. The latter is of utmost importance for the commercial viability and large-scale deployment of this technology.

This study aims to quantify systematically the optical losses and to estimate the change in the local and area-averaged light absorptance caused by the presence of cap-shaped gas bubbles evolving on the photoelectrode surface. The parameters systematically investigated included the bubble diameter, size distribution, contact angle, and projected surface area coverage. The light absorption by a bare photoelectrode without bubbles served as a reference. The results provide guidelines for selecting materials and coatings so as to minimize optical losses due to the inevitable presence of bubbles on large-scale photoelectrodes.

2. Background

Very few studies have analyzed the optical effects of bubbles on the performance of vertical or horizontal photoelectrodes.[2,11,12,19,20] Holmes-Gentle et al.[19] conducted experiments to study the optical losses due to a rising plume of O_2 gas bubbles evolving from a transparent vertical electrode consisting of a glass slide of surface area 15×15 mm^2 coated with fluorine-doped tin oxide (FTO) and immersed in an aqueous solution of 1 M NaOH. Collimated light was incident normally onto the electrode surface and its normal-hemispherical transmittance was recorded in the presence of bubbles using an integrating sphere. Then, the optical losses due to back-scattering from the bubble-covered electrode were calculated using the recorded transmittance since the electrode and electrolyte were non-absorbing. The average diameter of bubbles in the plume was about 45 μm. Optical losses up to 5% were reported due to scattering by the bubbles. Some of the strategies proposed to mitigate scattering losses included evolving fewer but larger bubbles and removing bubbles faster by flowing the electrolyte.

Njoka et al.[12] characterized the behavior of O_2 and H_2 gas bubbles on the surface of vertically-oriented Pt photoelectrodes by capturing macroscopic images to understand their effect on the performance of a tandem photoelectrochemical cell subject to normally incident radiation. The authors observed that H_2 bubbles tended to grow independently from one another, remained attached to the photoelectrode, and accumulated at its surface for longer periods of time compared to O_2 bubbles which tended to coalesce and rise rapidly. They reported that the size of bubbles on photoelectrodes was much larger than that on electrodes because of lower photocurrent densities in the photoelectrodes, with average departure diameter of H_2 bubbles about 1.7 mm while that of O_2 bubbles about 1.4 mm at photocurrent density of 9.6 mA cm^{-2}. Unfortunately, the bubble contact angle and surface area coverage were not reported. Overall, they estimated about 5% loss in the photocurrent density due to the presence of bubbles in a tandem photoelectrochemical cell.

Dorfi et al.[11] studied experimentally the losses in photocurrent density and external quantum efficiency (EQE) due to a single H_2 bubble attached to the surface of an upward-facing horizontal Si photocathode immersed in 0.5 M H_2SO_4 aqueous electrolyte. The bubble diameter varied from 200 μm to 2 mm while the contact angle of the bubble was either 20° or 50°. The authors used scanning photocurrent microscopy (SPCM) producing line scans of a normally incident laser beam of wavelength 532 nm over the bubble to determine experimentally the local variation of photocurrent density and EQE as compared to that of a Si photoelectrode without bubbles. Then, the experimental results were explained using predictions from a simple optical model based on Snell's law and accounting for bubble curvature but ignoring multiple reflections. The reduction in the photocurrent density caused by the presence of a bubble of diameter $D = 1$ mm reached up to 23%.

More recently, Kempler *et al.*[20] presented experimental measurements and ray-tracing simulations for the optical and electrochemical effects of H_2 bubbles attached to the surface of upward-facing horizontal 1×1 cm^2 Si photoelectrodes exposed to unpolarized monochromatic light ($\lambda = 630$ nm). They established experimentally that the photocurrent density decreased by up to 10% compared to that in a bare Si photoelectrode when a large fraction of the photoelectrode surface was covered with bubbles and not in direct contact with the electrolyte. Ray-tracing simulations were performed, generating line-scans of photocurrent density for a single bubble and a few equally-spaced monodisperse bubbles for a limited number of bubble contact angles ($\theta_c = 20°$, $60°$, and $90°$) and contact surface area coverages ($f_S = 0$ to 60%). Smaller bubbles were reported to cause smaller losses in photocurrent density as compared to larger bubbles for the same contact surface area coverage f_S. This was attributed to totally internally reflected rays from larger bubbles being redirected away from the photoelectrode surface. However, line-scan results do not fully capture the envisioned outdoor operation of photoelectrochemical cells where the entire photoelectrode surface and the numerous polydisperse bubbles are irradiated simultaneously.

Most previous studies investigated experimentally the effect of bubbles on the performance of photoelectrodes. They supported their experimental observations with relatively simple ray-tracing simulations considering a single bubble or a few monodisperse bubbles. However, Fig. 1 shows that in reality, numerous polydisperse bubbles are present on the photoelectrode surface. In addition, discussion of the effect of bubble contact angle on the optical losses was limited to a small range of contact angles. Indeed, the presence of micro- and nanostructures on the photoelectrode surface can change its wettability and thus the bubble contact angle.[21] In addition, the bubble contact angle may change due to photoinduced hydrophilicity[22] and Marangoni effects due to concentration gradients at the electrolyte/bubble interface.[23] Moreover, for generating sufficient H_2 gas to make the technology commercially viable, the photoelectrode should ideally be of a very large area,[20] whereas the photoelectrode areas simulated in most previous studies were at most cm-scale to match the electrode size used in their experiments.

This study aims to comprehensively investigate the optical losses caused by the presence of bubbles on horizontal photoelectrodes immersed in an aqueous electrolyte and exposed to normally incident monochromatic radiation. Monte Carlo ray-tracing method was utilized to predict the local and area-averaged absorptance in the photoelectrode. The simulations faithfully accounted for the interaction of the incident light on an infinitely large photoelectrode surface covered with either ordered or randomly distributed, monodisperse or polydisperse non-absorbing cap-shaped bubbles with a wide range of bubble diameters, contact angles, and projected surface area coverages. The spatial variations of the absorptance and its area-averaged value were systematically compared with those for the reference case of a bare photoelectrode immersed in electrolyte but without bubbles.

3. Analysis

3.1. Problem statement

Let us consider a square upward-facing horizontal Si photoelectrode of length L and thickness H immersed in an electrolyte and partially covered with a gas bubble of diameter D, contact angle θ_c, and projected diameter d_p such that $d_p = D$ for $0° \leq \theta_c < 90°$ and $d_p = D \sin(180° - \theta_c)$ for $90° \leq \theta_c < 180°$. The bubble/photoelectrode contact circle has a diameter d_c such that $d_c = d_p \sin \theta_c$ for $\theta_c \leq 90°$, and $d_c = d_p$ for $\theta_c > 90°$. The bubble projected surface area coverage f_A represents the fraction of the photoelectrode surface area covered with bubbles, as encountered by the normally incident photons. We also define the contact surface area coverage f_S as the fraction of the photoelectrode surface area covered by the bubble/photoelectrode interface. For a single bubble of contact angle θ_c and projected diameter d_p covering the photoelectrode surface area $L \times L$, $f_A = \pi d_p^2/4L^2$ and $f_S = \pi d_c^2/4L^2$. The opaque photoelectrode, of refractive and absorption indices n_p and k_p respectively, is immersed in a non-absorbing aqueous electrolyte and is subjected to collimated and normally incident radiation of wavelength λ. Fig. 2(a) shows the side view of the three-dimensional (3D) computational domain considered in the Monte Carlo ray-tracing simulations. It also shows the diameter d_t of the circle outside which total internal reflection occurs at the electrolyte/bubble interface.

3.2. Assumptions

To make the problem mathematically trackable, the following assumptions were made: (1) gas bubbles were cap-shaped. (2) Gas bubbles had a constant volume, constant contact angle, and were pinned (no sliding) to the surface of the photoelectrode. (3) Bubbles and electrolyte were non-absorbing with constant refractive indices denoted by n_b and n_e, respectively. (4) All surfaces were optically smooth so that specular reflection and refraction occurred at all interfaces according to Snell's law and Fresnel's equations. (5) Dimensions of the photoelectrode and of the bubbles were much larger than the wavelength λ of the incident radiation so that geometric optics was valid and wave effects could be neglected. (6) The photoelectrode was opaque so that all the photons entering it were absorbed. (7) Photoinduced hydrophilicity effects were neglected.

3.3. Monte Carlo ray-tracing method

The Monte Carlo ray-tracing method[24,25] was utilized to predict the normal-hemispherical reflectance R_{nh} and the local absorptance in an opaque photoelectrode immersed in a non-absorbing electrolyte and supporting gas bubbles on its top and subjected to normally incident monochromatic radiation. A step-by-step explanation of the computational procedure was given in our previous studies involving light transfer through a window supporting droplets on its front or back side.[26,27] Monodisperse or polydisperse cap-shaped bubbles were generated and Snell's law and Fresnel coefficients were calculated at the electrolyte/bubble, bubble/photoelectrode, and electrolyte/photoelectrode interfaces by using a similar methodology as
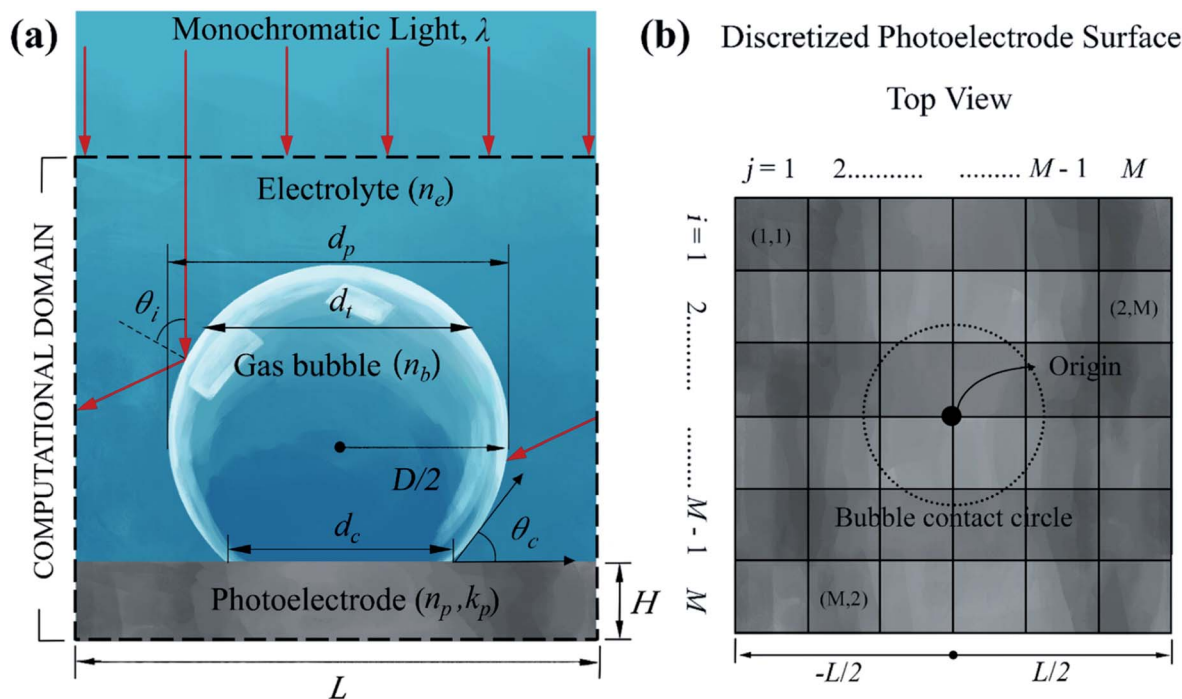
Fig. 2 (a) 2D cross-section of the 3D computational domain considered in Monte Carlo ray-tracing simulations for an infinite photoelectrode covered with monodisperse bubbles. Scattered photons reaching the sides of the system re-enter from the other side at the same height and travel in the same direction. (b) Photoelectrode surface discretized into $M \times M$ bins for computing the spatial variation of the local absorptance.

that used in our previous studies.[26,27] Fig. 2(a) illustrates the working of periodic boundary conditions such that photons reaching the sides of the computational domain re-enter from the opposite side at the same height and in the same direction. Such boundary conditions enable us to quantify the optical losses due to back-scattering of the incident photons by an infinitely large photoelectrode surface covered with bubbles. These losses can be characterized by the normal-hemispherical reflectance R_{nh} of the bubble-covered photoelectrode, as discussed in the next section. In addition, the performance of the photoelectrode can be compared with and without bubbles based on the local and area-averaged absorptance.

3.4. Modeling

Dorfi et al.[11] presented the following expression for the area-averaged photocurrent density $\bar{J}_{ph}$ (in A m^{-2}) generated in the photoelectrode immersed in an absorbing electrolyte

$$\bar{J}_{ph} = qIQE \frac{I}{(hc/\lambda)} (1 - R_{nh} - A_e - T_{nh}). \quad (1)$$

Here, q is the charge of an electron ($q = 1.60 \times 10^{-19}$ C), IQE is the internal quantum efficiency of the photoelectrode, I is the intensity of the incident radiation (in W m^{-2}), h is the Planck's constant (m^2 kg s^{-1}), c is the speed of light in vacuum (in m s^{-1}), λ is the wavelength of the incident radiation (in m), A_e is the fraction of the incident radiation lost due to absorption in the electrolyte before reaching the photoelectrode, and R_{nh} and T_{nh} are the normal-hemispherical reflectance and transmittance of the photoelectrode immersed in the electrolyte with or without

bubbles. However, eqn (1) seems erroneous. Indeed, for an absorbing electrolyte, the intensity of the radiation reaching the photoelectrode surface is $I(1 - A_e)$, a fraction of which is reflected or transmitted by the photoelectrode and is not converted into charge carriers in the photoelectrode. Therefore, the area-averaged photocurrent density $\bar{J}_{ph}$ when the electrolyte is partially absorbing the incident radiation should be expressed as

$$\bar{J}_{ph} = qIQE \frac{I}{(hc/\lambda)} (1 - A_e) (1 - R_{nh} - T_{nh}). \quad (2)$$

In addition, this expression assumes that the internal quantum efficiency IQE is the same at the bubble/photoelectrode interface and at the electrolyte/photoelectrode interface. However, among all the photons absorbed by the photoelectrode, those absorbed inside the bubble contact surface area may not all contribute to the photocurrent due to the absence of semiconductor–liquid junction where band-bending helps separate the generated charge carriers.

In the present study, the electrolyte is non-absorbing and the photoelectrode is opaque so that $A_e = 0$ and $T_{nh} = 0$. Therefore, optical losses were only caused by back-scattering at various interfaces and quantified by the normal-hemispherical reflectance R_{nh} of the bubble-covered photoelectrode. An area-averaged absorptance $\bar{A}$ of the photoelectrode can be defined as

$$\bar{A} = 1 - R_{nh} = N_a/N_i, \quad (3)$$

where N_i is the number of incident photons at wavelength λ and N_a is the number of photons absorbed in the photoelectrode. The absorptance for a photoelectrode without bubbles, with all other conditions remaining the same, is uniform over the photoelectrode surface, *i.e.*, $\bar{A} = A_0$ which can be written as

$$A_0 = 1 - R_{nh,0} = N_{a,0}/N_i, \tag{4}$$

where $N_{a,0}$ is the number of photons absorbed and $R_{nh,0}$ is the normal-hemispherical reflectance of the photoelectrode immersed in the electrolyte given by[24,25]

$$R_{nh,0} = \frac{(n_p - n_e)^2 + k_p^2}{(n_p + n_e)^2 + k_p^2}, \tag{5}$$

Here, n_p and n_e are, respectively, the refractive indices of the photoelectrode and the transparent electrolyte while k_p is the absorption index of the photoelectrode. The area-averaged absorptance normalized by the absorptance of the bare photoelectrode A_0, can be used to assess the optical losses caused by the presence of bubbles and defined as

$$\bar{A}/A_0 = (1 - R_{nh})/(1 - R_{nh,0}). \tag{6}$$

Eqn (6) indicates that the normalized area-averaged absorptance depends only on the normal-hemispherical reflectance R_{nh} of the photoelectrode.

Moreover, the presence of bubbles causes spatial variations in the photon flux absorbed in the photoelectrode. To determine the local absorptance, the photoelectrode surface was discretized into $M \times M$ square bins, as illustrated in Fig. 2(b). The location of each bin was identified by the (x,y) coordinates of its center, with the center of the photoelectrode surface serving as the origin $(0,0)$. By analogy with eqn (3), the local absorptance $A(x,y)$ in the bin at location (x,y) can be expressed as

$$A(x,y) = N_a(x,y)/N_i, \tag{7}$$

where $N_a(x,y)$ is the number of photons locally absorbed in the bin located at (x,y). The number $N_a(x,y)$ varied spatially from one bin to another due to redistribution of the incident radiation on the photoelectrode surface owing to scattering by the bubbles, and because of difference in the reflectances of the electrolyte/photoelectrode and bubble/photoelectrode interfaces. In the absence of bubbles, the number of photons absorbed is the same in all bins and equal to $N_{a,0} = N_i(1 - R_{nh,0})$. Then, the normalized local absorptance $A(x,y)/A_0 = N_a(x,y)/N_{a,0}$ represents the factor by which the local photon absorption is affected by the presence of bubbles.

3.5. Closure laws

All simulations were performed using normally incident monochromatic radiation at wavelength $\lambda = 630$ nm. This wavelength was chosen because scaled-up photoelectrochemical water splitting systems are envisioned to be driven by visible light.[4] The refractive index of the aqueous electrolyte solution was assumed to be that of water in the

visible, *i.e.*, $n_e = 1.33$.[20] Similarly, the refractive index of non-absorbing gas bubbles (H_2 or O_2) was assumed to be the same as that of vacuum, *i.e.*, $n_b = 1.0$.[20] In this study, crystalline Si was considered as the photoelectrode because of its relatively low bandgap, low cost, and abundance.[4] Its refractive and absorption indices at $\lambda = 630$ nm were taken as $n_p = 3.88$ and $k_p = 0.016$.[28]

The bubble diameter D was varied between 0.25 and 1.75 mm based on experimental results reported in ref. 11. The projected surface area coverage f_A was varied between 0 and 78.5% (*i.e.*, $\pi/4$) corresponding to the maximum possible value for monodisperse bubbles attached to the surface of a square photoelectrode. The contact angle θ_c was varied between $0°$ and $180°$ in increments of $15°$ to gain insights into the effects of surface wettability. For polydisperse bubbles, a normal distribution $f(D)$ of bubble diameter was assumed with a mean value of $\bar{D} = 1$ mm and standard deviation $\sigma = 0.25$ mm, and the length of the square photoelectrode was $L = 10$ mm with periodic boundary conditions. For monodisperse bubbles, different bubble diameters $D = 0.5$, 1, or 1.5 mm were considered and the photoelectrode length L was adjusted to achieve the desired value of projected surface area coverage f_A. In order to predict the normalized local absorptance $A(x,y)/A_0$ with a good spatial resolution at reasonable computational time, the length of the square photoelectrode was taken as $L = 1$ mm, and the photoelectrode surface was divided into $M \times M$ bins, with $M = 101$. Thus, all the bins were square and approximately 10 μm in length. Normalized local absorptance maps were generated for a single bubble with periodic boundary conditions to simulate monodisperse bubbles. Here, the diameter of the bubble was varied to achieve the desired projected surface area coverage. Finally, all the results reported correspond to a total number of incident photons $N_i = 10^7$ necessary to achieve numerical convergence.

4. Results and discussion

This section presents the effects of (1) bubble diameter D, (2) bubble size distribution $f(D)$, (3) contact angle θ_c, and (4) projected surface area coverage f_A on the normal-hemispherical reflectance R_{nh} and on the local $A(x,y)$ and area-averaged $\bar{A}$ absorptance of a horizontal Si photoelectrode covered with H_2 or O_2 bubbles.

4.1. Normal-hemispherical reflectance

4.1.1. Effect of bubble diameter, polydispersity, and spatial distribution. Fig. 3(a) plots the normal-hemispherical reflectance R_{nh} as a function of contact angle θ_c for monodisperse bubbles with projected surface area coverage f_A equal to 40% or 78.5% and diameter D equal to 0.5, 1.0, or 1.5 mm. Here, the length of the photoelectrode L was adjusted to achieve the desired projected surface area coverage f_A. It is evident that the bubble diameter D had no effect on the normal-hemispherical reflectance R_{nh} for any given projected surface area coverage f_A and bubble contact angle θ_c. In fact, the reflectance R_{nh} increased systematically with increasing projected surface area
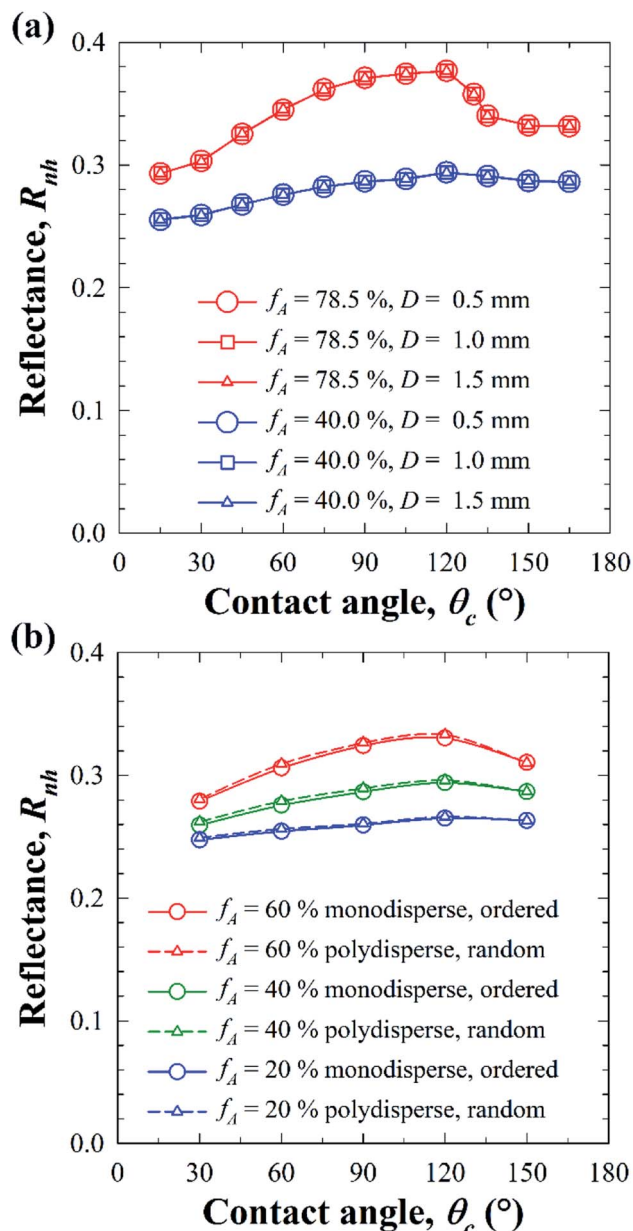
The photoelectrode length L was equal to 10 mm. Fig. 3(b) establishes that the bubble size distribution and their spatial distribution did not have any significant effect on R_{nh} for given values of projected surface area coverage f_A and contact angle θ_c. Similar trends were obtained for non-absorbing droplets on a transparent window.[26,27]

Overall, Fig. 3 establishes that for a non-absorbing electrolyte, the bubble diameter D and size distribution $f(D)$ had no effect on the normal-hemispherical reflectance R_{nh} of the photoelectrode. Instead, R_{nh} was only dependent on the bubble contact angle θ_c and projected surface area coverage f_A, i.e., $R_{\text{nh}} = R_{\text{nh}}(f_A, \theta_c)$.

4.1.2. Effect of bubble contact angle θ_c. Fig. 4 presents the normal-hemispherical reflectance R_{nh} as a function of bubble contact angle θ_c for projected surface area coverage f_A ranging from 0% to 78.5%. The reflectance R_{nh} of a bare Si photoelectrode (i.e., $f_A = 0\%$) immersed in electrolyte and that of a Si photoelectrode covered with a 1 mm thick gas film (i.e., $f_A = 100\%$) sandwiched between the photoelectrode and the electrolyte are also shown as references. Here again, it is evident that the reflectance R_{nh} increased with increasing projected surface coverage f_A for any given contact angle θ_c due to backscattering caused by various interfaces. Even though the incident radiation was normal to the photoelectrode surface, the angle of incidence θ_i at the electrolyte/bubble interface – defined from the outward normal to the bubble surface [see Fig. 2(a)] – varied due to the bubble curvature. In fact, it varied between 0° and 90° for $\theta_c \leq 90°$ and between 0° and $180° - \theta_c$, for $\theta_c > 90°$. According to Snell's law, total internal reflection

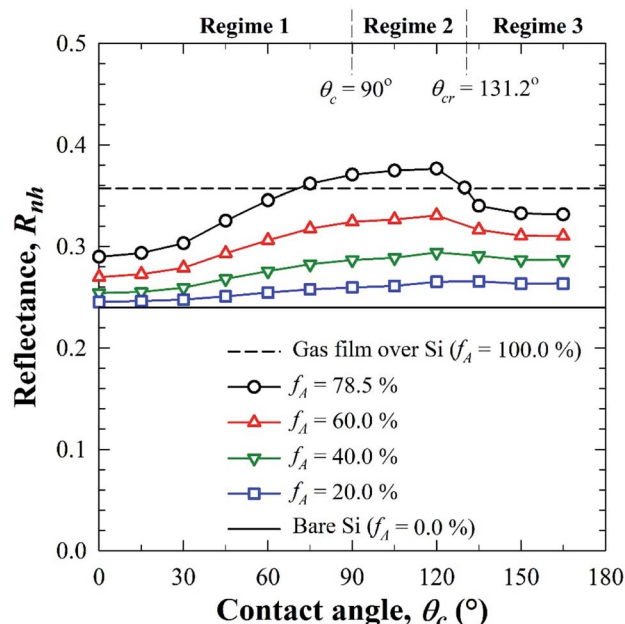Fig. 3 (a) Normal-hemispherical reflectance R_{nh} of a photoelectrode covered with bubbles as a function of contact angle θ_c for (a) ordered monodisperse bubbles with different diameter D and projected surface area coverage $f_A = 40\%$ or 78.5%; (b) ordered monodisperse bubbles and randomly distributed polydisperse bubbles with normal distribution with $\overline{D} = 1$ mm and $\sigma = 0.25$ mm for projected surface area coverage $f_A = 20\%$, 40%, or 60%.

Fig. 4 Normal-hemispherical reflectance R_{nh} as a function of contact angle θ_c for different projected surface area coverage f_A. The reflectance R_{nh} of a bare Si photoelectrode (i.e., $f_A = 0\%$) immersed in electrolyte, and that of an Si photoelectrode covered with a 1 mm thick gas film (i.e., $f_A = 100\%$) immersed in electrolyte are also shown as references.

coverage f_A for any given contact angle θ_c. However, the bubble contact angle θ_c had a more complex effect on R_{nh}, as discussed later in this study.

Fig. 3(b) compares the normal-hemispherical reflectance R_{nh} of a photoelectrode surface covered with either ordered monodisperse bubbles (diameter $D = 1$ mm) or randomly distributed polydisperse bubbles (normal size distribution with $\overline{D} = 1$ mm and $\sigma = 0.25$ mm) as a function of bubble contact angle θ_c for projected surface area coverage f_A equals to 20%, 40%, and 60%.

occurs when the angle of incidence θ_i is such that $\theta_i > \sin^{-1}(n_b/n_e)$ where n_b and n_e are the refractive indices of the gas and the electrolyte, respectively. Since the range of θ_i depends on the bubble contact angle θ_c, total internal reflection occurred when θ_c was smaller than the critical angle for total internal reflection given by

$$\theta_{cr} = 180° - \sin^{-1}(n_b/n_e) = 131.2°. \quad (8)$$

In particular, for $\theta_c > \theta_{cr}$, no incident photon was internally reflected at the electrolyte/bubble interface. Thus, for a given projected surface area coverage f_A, three distinct optical regimes can be identified, namely (a) Regime 1 corresponding to contact angles $0° \leq \theta_c < 90°$, (b) Regime 2 with $90° \leq \theta_c < \theta_{cr}$, and (c) Regime 3 such that $\theta_c \geq \theta_{cr}$, as illustrated by the ray-tracing diagrams of Fig. 5.

Regime 1, $0° \leq \theta_c < 90°$. As θ_c increased from $0°$ to $90°$ for a given projected surface area coverage, the contact surface area coverage f_S ($= \pi d_c^2/4L^2$) increased. Therefore, more incident rays reached the bubble/photoelectrode interface rather than the electrolyte/photoelectrode interface and were more likely to get reflected back due to the large refractive index mismatch. Therefore, in Regime 1, the normal-hemispherical reflectance R_{nh} increased with increasing contact angle θ_c. Also, since $\theta_c < \theta_{cr}$, some of the photons were totally internally reflected at the electrolyte/bubble interface and contributed to the reflectance R_{nh}. However, their contribution did not change significantly with θ_c since the annular region between diameters d_t and d_p inside which total internal reflection occurred remained unchanged in this regime and most of the internally reflected photons were scattered forward [see Fig. 5(a)] and eventually reached the surface of the photoelectrode regardless of the contact angle.

Regime 2, $90° \leq \theta_c < \theta_{cr}$. In Regime 2, the contact surface area coverage f_S was equal to the projected surface area coverage f_A since $d_c = d_p$. However, for a given value of f_A, the annular region between diameters d_t and d_p, in which total internal reflection occurred, decreased as the contact angle θ_c increased due to increase in d_t up to $d_t = d_p$ at contact angle $\theta_c = \theta_{cr}$. Then, fewer photons were totally internally reflected as compared to Regime 1 and more of them were refracted across the bubble/electrolyte interface towards the bubble/photoelectrode interface. Therefore, the contribution of total internal reflection to the reflectance R_{nh} decreased while that of reflection at the bubble/photoelectrode interface increased with increasing contact angle. Thus, the reflectance R_{nh} increased slightly with increasing contact angle up to $\theta_c = 120°$ and then decreased beyond due to negligible contribution from total internal reflection.

Regime 3, $\theta_c \geq \theta_{cr}$. In Regime 3 also, $d_c = d_p$ and $f_S = f_A$ but total internal reflection did not occur at the electrolyte/bubble interface since $\theta_c > \theta_{cr}$ [see Fig. 5]. Therefore, the normal-hemispherical reflectance R_{nh} was only due to contribution from reflection at the bubble/photoelectrode or electrolyte/photoelectrode interfaces. Thus, R_{nh} dropped off at $\theta_c \approx \theta_{cr}$, and remained nearly constant beyond, since the contact surface area coverage f_S was constant for a given f_A and the number of photons encountering the bubble/photoelectrode interface remained unchanged with increasing contact angle.

Finally, it is interesting to note that for all projected surface area coverages f_A considered, the magnitude of the normal-hemispherical reflectance R_{nh} at contact angle $\theta_c = 0°$ (Regime 1) – when total internal reflection dominated – was smaller than that at $\theta_c = 165°$ (Regime 3) when reflection at the bubble/photoelectrode interface dominated. These limiting cases illustrate the interplay between total internal reflection at the electrolyte/bubble interface and reflection at the bubble/
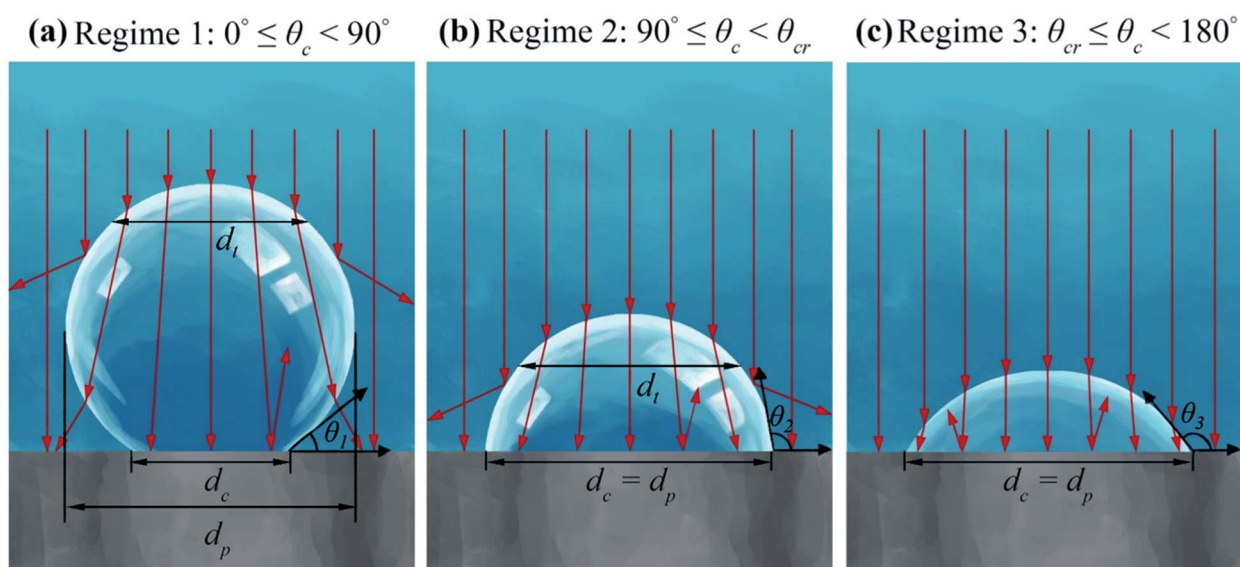

Fig. 5 Schematic illustrating the change in the contributions from contact surface area coverage ($=\pi d_c^2/4L^2$) and total internal reflection to the normal hemispherical reflectance R_{nh} based on the contact angle θ_c in (a) Regime 1, (b) Regime 2, and (c) Regime 3 identified in Fig. 4.

photoelectrode interface for a horizontal photoelectrode under normal incidence.

4.1.3. Effect of bubble projected surface area coverage f_A. Fig. 6(a) plots the normal-hemispherical reflectance R_{nh} as a function of projected surface area coverage f_A for contact angles θ_c equal to 30°, 60°, 120°, and 150° corresponding to the optical Regimes 1, 2, and 3 described previously. The figure also shows the reflectance $R_{nh,0}$ of a bare photoelectrode immersed in the electrolyte [eqn (5)] and the reflectance $R_{nh,gf}$ of the photoelectrode in contact with a non-absorbing gas film with the same thickness as the bubble diameter and given by[24,25]

$$R_{nh,gf} = \rho_{eb} + \frac{\rho_{bp}(1 - \rho_{eb})^2}{1 - \rho_{eb}\rho_{bp}}, \quad (9)$$

where ρ_{ij} is the reflectance at the optically smooth interface between media i and j under normal incidence, given by[24,25]

$$\rho_{ij} = \frac{(n_i - n_j)^2 + (k_i - k_j)^2}{(n_i + n_j)^2 + (k_i + k_j)^2}, \quad (10)$$

where n_i and n_j are respectively the refractive indices of media i and j, while k_i and k_j are their absorption indices, respectively. The subscripts e, b and p refer to the electrolyte, the bubble, and the photoelectrode, respectively.

In Regimes 1 and 2, R_{nh} increased non-linearly with f_A while in Regime 3, it increased linearly. This can be explained by analyzing the respective contributions of total internal reflection at the electrolyte/bubble interface and reflection at the bubble/photoelectrode interface to the total optical losses.

Fig. 6(b) schematically compares the illumination over a photoelectrode covered with bubble having small or large projected surface area coverage f_A for the same bubble contact angle θ_c in Regime 1 or 2. It illustrates that the losses due to total internal reflection increased with increasing projected surface area coverage f_A. In fact, at low projected surface area coverage f_A, many photons eventually reached the photoelectrode surface after total internal reflection. By contrast, for large projected surface area coverage f_A, many photons were back-scattered upon total internal reflection at the electrolyte/bubble interface. The losses further increased with increasing f_A since the contact surface area coverage f_S increased and more rays encountered the bubble/photoelectrode interface rather than the electrolyte/photoelectrode interface. Therefore, in Regimes 1 and 2, the normal-hemispherical reflectance R_{nh} increased non-linearly with projected surface area coverage f_A. Note that for a projected surface area coverage $f_A = 78.5\%$, the normal-hemispherical reflectance R_{nh} in Regime 2 even surpassed that of a gas film corresponding to $f_A = 100\%$. This can be attributed to the additional back-scattering losses from total internal reflection arising from the bubbles' curvatures.

On the other hand, in Regime 3 for contact angles $\theta_c \geq \theta_{cr}$, total internal reflection was absent and R_{nh} could be approximated as the weighted sum of the reflectances (i) $R_{nh,0}$ of the photoelectrode in contact with the electrolyte [eqn (5)] and (ii) $R_{nh,gf}$ of the electrode covered with a gas film [eqn (9)], i.e.,
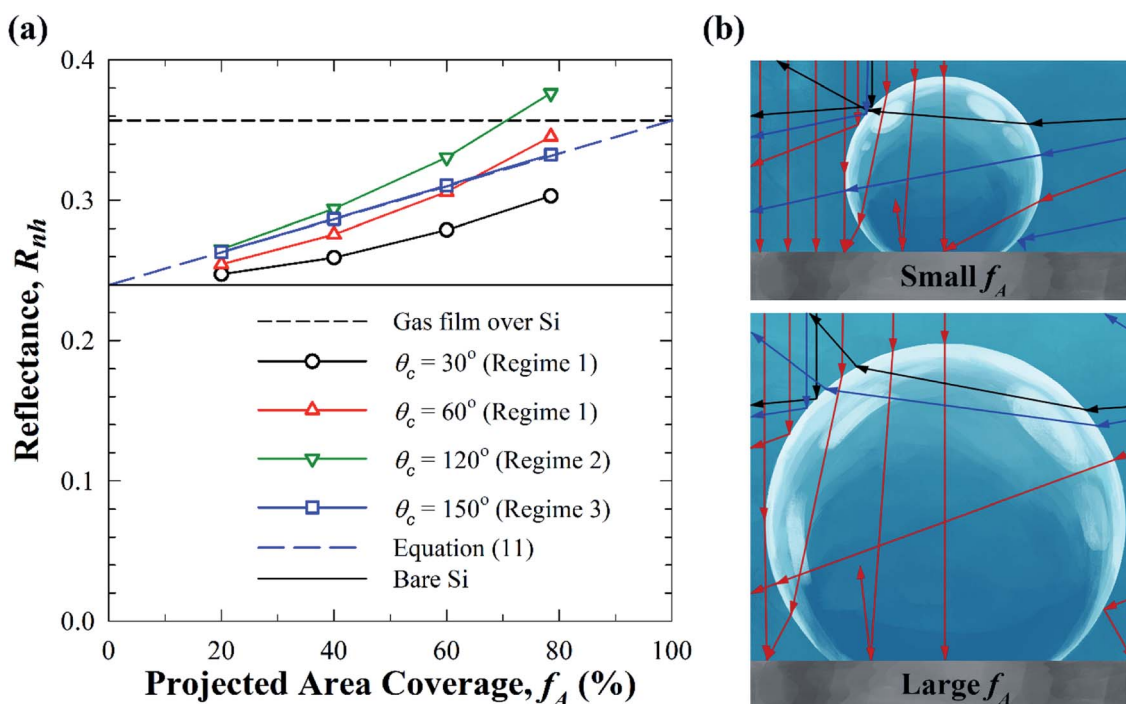
$$R_{nh} = R_{nh,0}(1 - f_A) + R_{nh,gf}f_A. \quad (11)$$

Fig. 6 (a) Normal-hemispherical reflectance R_{nh} as a function of projected surface area coverage f_A for different contact angles θ_c in Regimes 1, 2, and 3. The reflectance R_{nh} of a bare Si photoelectrode (i.e., $f_A = 0\%$) immersed in electrolyte and that for an Si photoelectrode completely covered with a gas film (i.e., $f_A = 100\%$) and immersed in electrolyte are also shown. (b) Ray-tracing diagrams showing an increase in the total internal reflection losses as f_A increased.

Fig. 6(a) establishes that in Regime 3, predictions of the reflectance R_{nh} by eqn (11) were in excellent agreement with results from Monte Carlo ray-tracing simulations.

All the results correspond to situations when bubbles were attached to the surface of the photoelectrode and no bubbles were present in the volume of the electrolyte above the photoelectrode surface. In practice, this situation corresponds to the onset of the photoelectrochemistry and bubble nucleation. At later times, bubbles may be present in the electrolyte volume and may increase the back-scattering losses and affect the direction of rays incident on the photoelectrode surface covered with bubbles. On the other hand, some of the reflected radiation from the bubble-covered photoelectrode surface may also be back-scattered towards the photoelectrode after interaction with the bubbles in the volume. Note, however, that large bubbles in the non-absorbing electrolyte scatter visible light mostly in the forward direction.[24,29] The overall effect of bubbles in the electrolyte is complicated and its investigation falls beyond the scope of this study.

The results for the normal-hemispherical reflectance R_{nh} can be used to compare the optical losses in a photoelectrode with and without bubbles quantified by the normalized area-averaged absorptance. On the other hand, more detailed simulations are necessary for predicting the normalized local absorptance as discussed in the following sections.

4.2. Normalized area-averaged absorptance $\bar{A}/A_0$

Fig. 7(a) presents the normalized area-averaged absorptance $\bar{A}/A_0$ [eqn (6)] as a function of bubble contact angle θ_c for different projected surface area coverage f_A. It indicates that the optical losses caused by the presence of bubbles can be as high as 18% for $f_A = 78.5\%$ and $\theta_c = 120°$. Fig. 7(a) also establishes that the losses were the smallest for $\theta_c = 0°$ for any given surface area coverage f_A. In fact, for contact angle θ_c up to 30°, the optical losses were less than 10% for any considered value of f_A. Therefore, hydrophilic surfaces should be used to minimize the losses due to back-scattering by the bubbles. For silicon, hydroxyl-terminated Si surfaces have a high wettability, which decreases the bubble contact angle θ_c and decreases the contact surface area coverage f_S.[20] The wettability of photoelectrodes can also be controlled by micro/nanostructuring their surfaces.[20]

Fig. 7(b) plots the normalized area-averaged absorptance $\bar{A}/A_0$ as a function of the projected surface area coverage f_A for different contact angles θ_c corresponding to the three different optical Regimes 1 to 3 previously identified. It indicates that optical losses increased with increasing f_A for all values of θ_c considered. In addition, the kinetic and ohmic losses also increase with increasing projected area coverage since the bubble contact surface area coverage increases.[10] The kinetic and ohmic losses are usually estimated in terms of their respective activation and ohmic overpotentials.[10] Typically, the kinetic losses dominate over the ohmic losses at low current densities while the opposite prevails for high current densities.[10] For photoelectrochemical applications, the current densities are usually relatively small and therefore, the ohmic losses are negligible compared with kinetic losses.[11] The kinetic
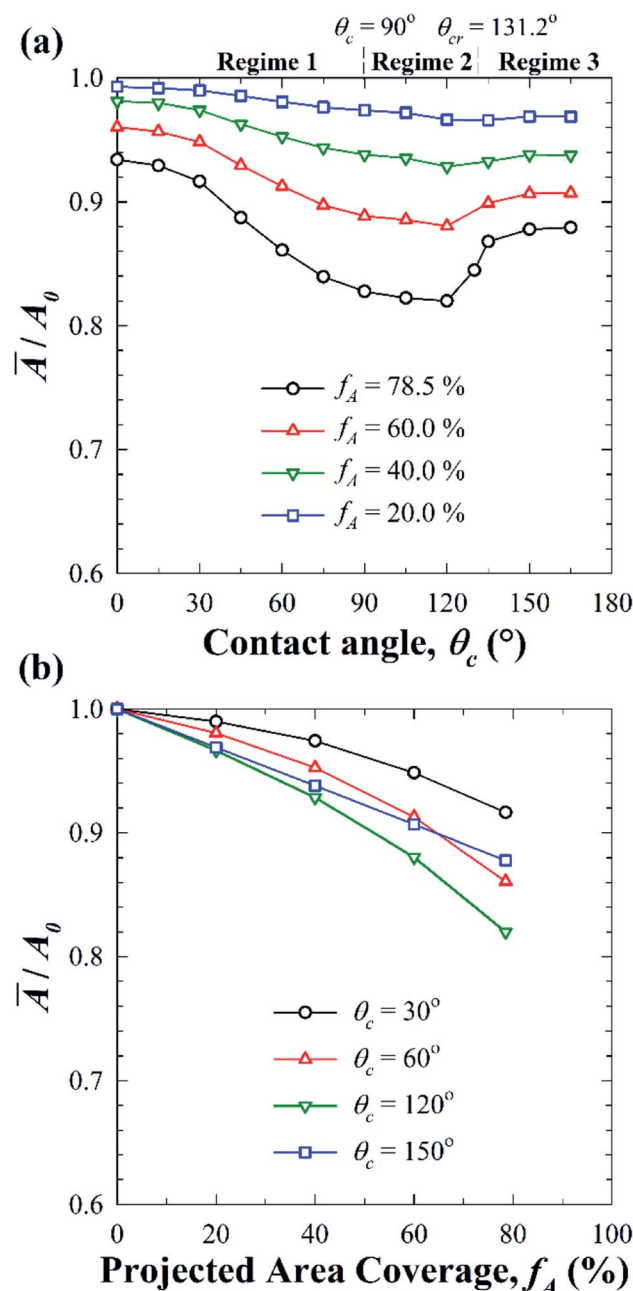

Fig. 7 Normalized area-averaged absorptance $\bar{A}/A_0$ as a function of (a) the bubble contact angle θ_c for different projected surface area coverages and (b) the projected surface area coverage f_A for different bubble contact angles corresponding to Regimes 1 to 3.

losses are estimated to be between 0 and 2% for bubble contact surface area coverages f_S up to 40%.[16] Increasing the contact surface area coverage also decreases the photoelectrode surface exposed to the electrolyte and available for the redox reactions. Due to this loss of semiconductor–liquid junction, some of the generated charge carriers directly below the bubble contact surface area may not contribute to the photocurrent. Overall, the photoelectrode performance can be improved by reducing the bubble coverage by facilitating the early departure of

Published on 10 January 2022. Downloaded by University of California - Los Angeles on 1/19/2022 4:31:24 PM.

bubbles from the surface with the help of convection in the electrolyte or the use of surfactants.[10,19,30,31]

The results presented in this study show good qualitative agreement with experiments reported in the literature.[11,20] First, Kempler et al.[20] estimated around 10% loss in the photocurrent density due to substantial gas coverage on the photoelectrode surface with bubble advancing contact angle > 70°. These results agree well with the optical loss predictions from our simulations for bubbles with projected surface area coverage f_A = 60% and the contact angle $\theta_c = 75°$ at the same wavelength of incident radiation. Second, the benefits of using hydrophilic coatings on the surface of the photoelectrode as previously discussed are substantiated by the experimental results from Kempler et al.[20] On the other hand, our predictions differ from the experimental results by Dorfi et al.,[11] who concluded that smaller bubbles were preferable over larger bubbles to minimize optical losses. By contrast, our study demonstrated that the bubble size had no effect on the photoelectrode absorptance for a given projected surface area coverage f_A. However, the bubble projected surface area coverage in the study by Dorfi et al.[11] increased with increasing bubble size. Also, the authors used a small photoelectrode (area = 0.25 cm²) resulting in optical losses from the edges of the photoelectrode. By contrast, edge effects were negligible for the large photoelectrodes simulated in our study and light scattered by one bubble interacted with neighboring bubbles while keeping the projected area coverage constant; hence the discrepancies.

4.3. Normalized local absorptance $A(x,y)/A_0$

Spatial variations in the local absorbed photon flux due to the presence of bubbles can be visualized using the normalized local absorptance map of $A(x,y)/A_0$.

4.3.1. Effect of bubble contact angle θ_c. Figs. 8(a) and 8(b) show respectively the side and top views of an upward-facing photoelectrode exposed to normally incident collimated radiation and featuring a gas bubble attached to its surface with a contact angle θ_c. Fig. 8(b) also shows the x-axis, a centerline CL, and three rings corresponding to (i) the bubble's projected radius $r_p = d_p/2$, (ii) the contact radius r_c of the bubble covering the photoelectrode such that $r_c = d_c/2$, and (iii) the radius r_t of the circle outside which total internal reflection occurs on the bubble, given by $r_t = r_p \sin(180° - \theta_{cr})$ where θ_{cr} is given by eqn (8). The interaction of the incident photons with interfaces identified by these three rings influenced the spatial distribution of absorbed light intensity in the photoelectrode.

Fig. 8 shows the normalized local absorptance maps for bubble contact angle (c) $\theta_c = 30°$, (d) $\theta_c = 60°$, (e) $\theta_c = 90°$, and (f) $\theta_c = 150°$ and projected surface area coverage $f_A = 40\%$. As a reference, the normalized local absorptance for a bare photoelectrode submerged in the electrolyte was $A(x,y)/A_0 = 1$. Outside the projected bubble radius r_p, $A(x,y)/A_0$ was larger than 1.0 for bubbles with $\theta_c < \theta_{cr}$ (optical Regimes 1 and 2) due to light concentration after scattering by the bubbles. The thickness of this concentration region shrank as θ_c increased since the photons traveled relatively shorter distance to reach the photoelectrode surface after total internal reflection at the

surface of one or more bubbles. The concentration region eventually disappeared for $\theta_c > \theta_{cr}$ when total internal reflection was absent. Inside the disk such that $r < r_p$, the ratio $A(x,y)/A_0$ was less than unity and its spatial variation for different contact angles θ_c can be explained by considering the differences in optics brought about by the change in the relative positions of the rings of radii r_t, r_c, and r_p as well as by the changing bubble contact angle. Fig. 8(c) shows the results for bubble contact angle $\theta_c = 30°$, where the contact radius r_c was smaller than the radius r_t of the circle outside which total internal reflection prevailed since $\theta_c < 180° - \theta_{cr}$. Most of the incident photons in the annular region $r_t \leq r \leq r_p$ were totally internally reflected at the electrolyte/bubble interface while those inside the disk of radius r_t were mostly refracted towards the photoelectrode surface. The photons reaching the photoelectrode surface encountered the bubble/photoelectrode interface inside the disk of radius r_c, leading to $A(x,y)/A_0 < 1$ due to reflection caused by the large refractive index mismatch between the bubble(s) and the photoelectrode. Outside r_c, the photons encountered the electrolyte/photoelectrode interface, where $A(x,y)/A_0 < 1$ in the annular region $r_c \leq r \leq r_p$ due to reduced local photon flux as compared to a bare photoelectrode owing to scattering by the bubbles. Finally, as previously discussed, light concentrated outside the projected bubble radius such that $A(x,y)/A_0 > 1$ for $r \geq r_p$. These results were typical for contact angles in the range $0 \leq \theta_c \leq 180° - \theta_{cr}$, since the relative positions of the three rings remained the same i.e., $r_c < r_t < r_p$. Fig. 8(d) corresponds to $\theta_c = 60°$, where the radius of the contact circle r_c was greater than the radius r_t since $\theta_c > 180° - \theta_{cr}$. Most of the photons incident in the region $r < r_t$ were refracted and got reflected at the bubble/photoelectrode interface resulting in normalized local absorptance $A(x,y)/A_0 < 1$. In the annular region $r_t \leq r \leq r_p$, $A(x,y)/A_0$ remained less than unity due to reduced local photon flux owing to total internal reflection. These results were representative of contact angles in the range $180° - \theta_{cr} \leq \theta_c \leq 90°$. Fig. 8(e) shows the results for contact angle $\theta_c = 90°$. Here, the contact and projected bubble radii were equal, i.e., $r_c = r_p$ but r_c was larger than r_t, the radius for total internal reflection at the bubble surface. Thus, in the region $r < r_p$, all refracted photons reached the bubble/photoelectrode interface where reflection due to high refractive index mismatch led to $A(x,y)/A_0 < 1$. In the annular region $r_t \leq r \leq r_p$, $A(x,y)/A_0$ decreased further due to the reduction in the local photon flux owing to total internal reflection. These results were typical of contact angles in the optical Regime 2 i.e., $90° \leq \theta_c \leq \theta_{cr}$ as discussed earlier. Finally, Fig. 8(f) shows that for contact angle $\theta_c = 150°$, the local photon flux was nearly uniform because total internal reflection did not occur at the electrolyte/bubble interface, since $\theta_c > \theta_{cr}$. Here also, $r_c = r_p$ and $A(x,y)/A_0$ was smaller than 1 for $r < r_c$ due to reflection at the bubble/photoelectrode interface. The photons incident outside r_c reached the electrolyte/photoelectrode interface leading to $A(x,y)/A_0 = 1$. These results were representative of all contact angles $\theta_c > \theta_{cr}$ corresponding to the optical Regime 3.

Overall, the results establish that the presence of bubbles caused significant local variation in the absorbed photon flux in the photoelectrode. This variation inside and outside the
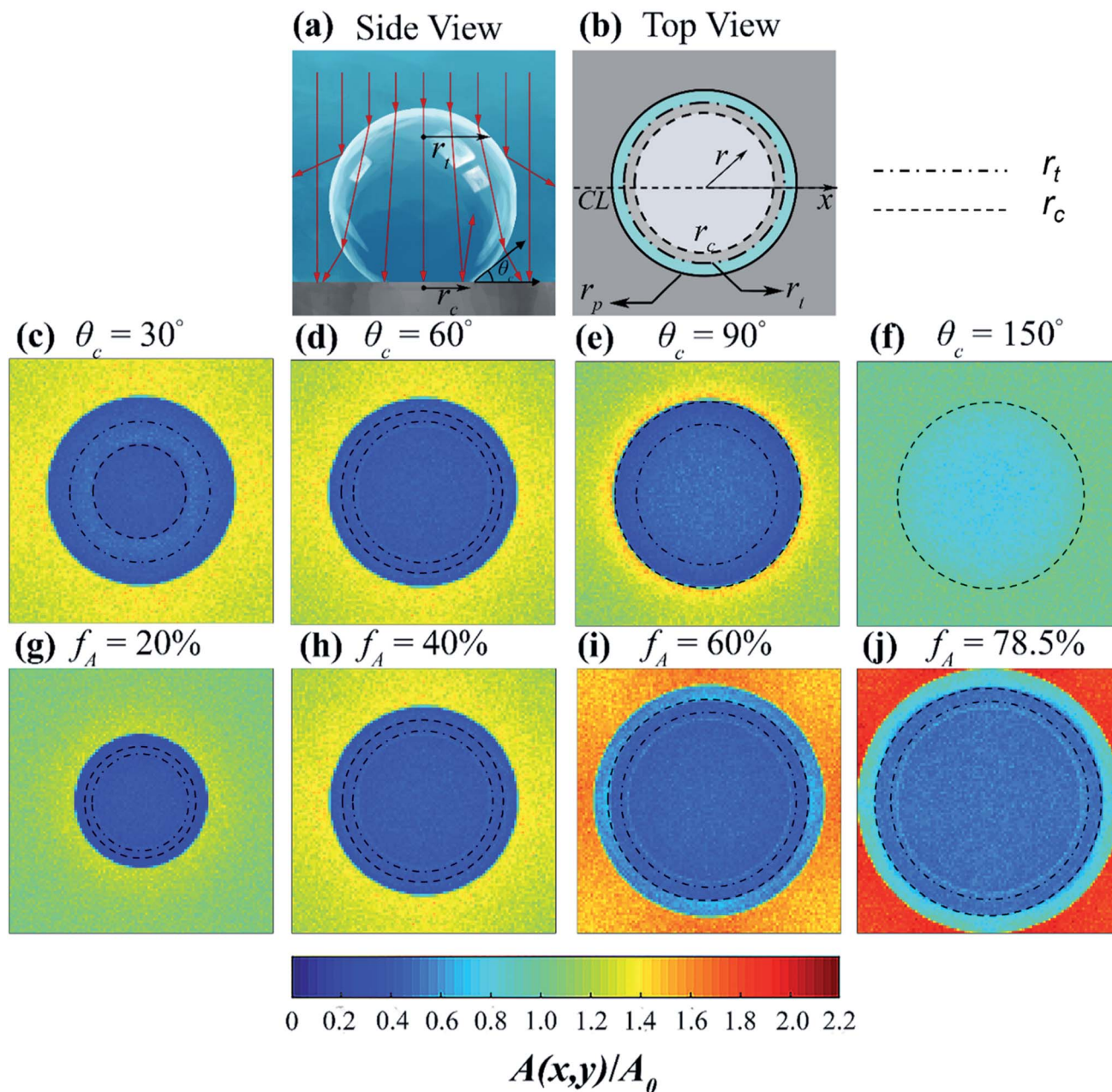
Fig. 8 (a) Side view of a photoelectrode covered with a bubble. (b) Top view of the photoelectrode surface, showing the x-axis, the centerline CL, and the three rings of radii r_t, r_c, and r_p. Spatial variation of the normalized local absorptance $A(x,y)/A_0$ for contact angle (c) $\theta_c = 30°$, (d) $\theta_c = 60°$, (e) $\theta_c = 90°$, and (f) $\theta_c = 150°$ at projected surface area coverage $f_A = 40\%$ and for projected surface area coverages (g) $f_A = 20\%$, (h) $f_A = 40\%$, (i) $f_A = 60\%$, and (j) $f_A = 78.5\%$ at contact angle $\theta_c = 60°$.

projected footprint of the bubble was explained by analyzing the different optical phenomena occurring for different bubble contact angles and contact surface area coverages. The absorbed photon flux was concentrated in the rim of the bubble outside the projected radius r_p, while inside, it was always less than that in a bare photoelectrode. The results also indicate that even though hydrophilic surfaces should be preferred to minimize the optical losses, the bubbles generated on such surfaces can scatter the photons far from their incident location. This could potentially be an issue when conducting experiments

with small (mm-scale) photoelectrodes due to photons being totally internally reflected away from the photoelectrode. Then, the optical losses will be larger than those predicted in this study.

4.3.2. Effect of bubble projected surface area coverage f_A. Fig. 8 also presents the normalized local absorptance maps $A(x,y)/A_0$ for projected surface area coverage f_A equal to (g) 20%, (h) 40%, (i) 60%, and (j) 78.5% for contact angle $\theta_c = 60°$. It indicates that $A(x,y)/A_0$ became increasingly concentrated (up to a factor of 2) outside the projected footprint of the bubble as f_A

increased due to total internal reflection and the increased proximity of the bubbles [see Fig. 6(b)]. Such high local concentration of incident radiation due to scattering from bubbles can lead to corrosion of the photoelectrode, thereby reducing its lifetime.[32] Inside the projected footprint of the bubble, the spatial variation of $A(x,y)/A_0$ can be explained with the help of rings of radii r_c, r_t, and r_p, as discussed earlier for $\theta_c = 60°$ and $f_A = 40\%$ [Fig. 8(d)]. Overall, $A(x,y)/A_0$ increased at all locations inside the projected footprint of the bubble as f_A increased due to scattered photons from neighboring bubbles ultimately reaching the bubble/photoelectrode interface.

4.3.3. Comparison of normalized local absorptance. Fig. 9 plots the normalized local absorptance $A(x,y)/A_0$ as a function of the normalized location of the center of the bins x/r_p along the centerline CL of the bubble [see Fig. 8(a)] for (a) contact angles $\theta_c = 30°, 60°, 90°$, and $150°$ with projected surface area coverage $f_A = 40\%$ and for (b) projected surface area coverages $f_A = 20\%$, 40%, 60% and 78.5% with contact angle $\theta_c = 60°$. Fig. 9(a) shows that for $\theta_c = 30°, 60°$, and $90°$, the presence of the bubbles concentrated the local absorptance up to 1.5 times in a region outside the bubble projected diameter. Inside, $A(x,y)/A_0$ decreased sharply to $\sim$0.4 and was nearly identical for all contact angles considered. However, no such concentration or sharp drop-off was observed for $\theta_c = 150°$ due to the absence of total internal reflection. Similarly, Fig. 9(b) compares the magnitude of normalized local absorptance $A(x,y)/A_0$ for different values of f_A. Here, the projected bubble radius r_p increased with increasing f_A for the same dimensions of the photoelectrode surface. Fig. 9(b) shows that the magnitude of $A(x,y)/A_0$ increased with f_A both inside and outside the projected footprint of the bubble, as discussed earlier for Fig. 8(g)–(j). Note that the spikes observed in the plots were due to the small local variation in the number of incident photons due to random incident locations generated in the Monte Carlo ray-tracing simulations.

4.3.4. Comparison of absorption inside and outside bubble contact surface area. Fig. 10 plots the fraction of incident radiation reflected and absorbed inside or outside the bubble contact surface area as a function of bubble contact angle for different projected surface area coverages (a) $f_A = 20\%$, (b) $f_A = 40\%$, (c) $f_A = 60\%$, and (d) $f_A = 78.5\%$. Fig. 10 shows that most of the absorption still took place in the photoelectrode area in contact with the electrolyte even for high projected area coverage f_A, provided the contact angle was small. Thus, hydrophilic photoelectrodes with small bubble contact angle are preferable since they ensure that most of the photoelectrode surface area remains in contact with the electrolyte so that the generated charge carriers participate in the water splitting reaction. However, for large projected area coverage f_A, as the contact angle increased, the amount of absorption inside the bubble contact surface area exceeded that outside it. Such a situation is undesirable since most of the generated charge carriers may not be able to participate in the water splitting reaction in the absence of semiconductor–liquid junction. The results presented in Fig. 10 also have implications in selecting a suitable anti-reflective coating for the photoelectrode surface. Indeed, if the projected surface area coverage and the bubble
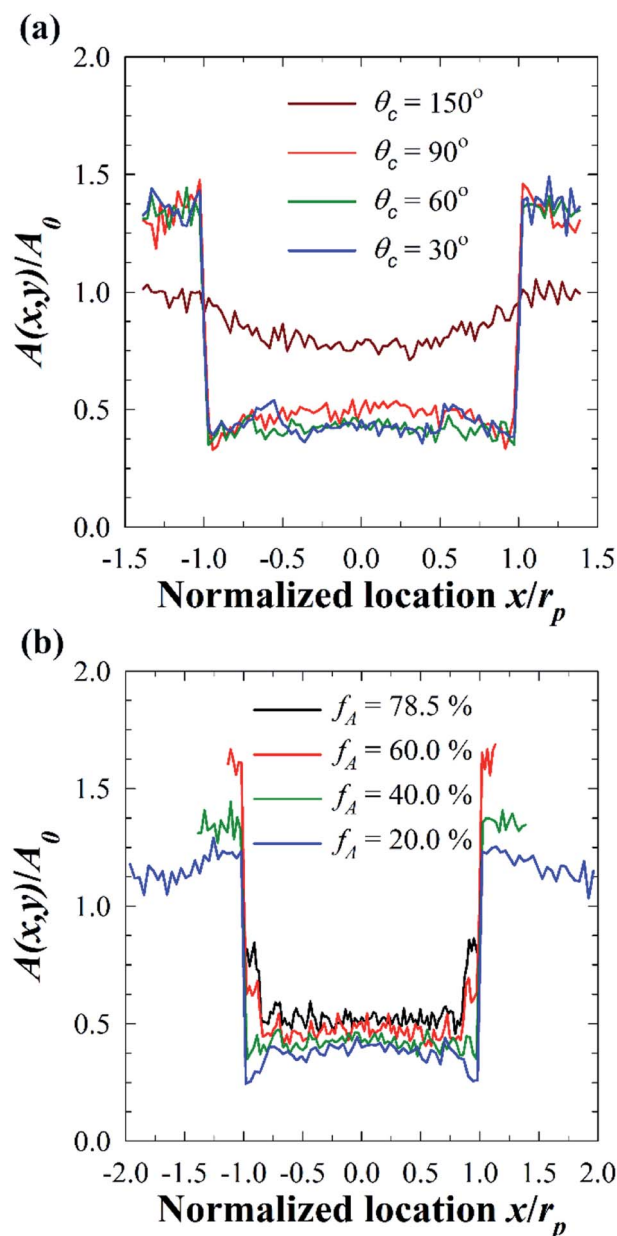

Fig. 9 Normalized local absorptance $A(x,y)/A_0$ along the centerline of a bubble as a function of normalized location x/r_p for (a) different contact angles θ_c with projected surface area coverage $f_A = 40\%$ and (b) different projected surface area coverages f_A with contact angle $\theta_c = 60°$.

contact angle are large, it is appropriate to choose an anti-reflective coating aimed at reducing the reflectance of the bubble/photoelectrode interface rather than that of the electrolyte/photoelectrode interface, since most of the photons are absorbed inside the bubble contact surface area. For example, at $f_A = 78.5\%$ and contact angle $\theta_c = 90°$, the contact surface area coverage $f_S = f_A$ and most of the incident photons encounter the bubble/photoelectrode interface. However, for a hydrophilic photoelectrode surface, the bubble contact surface area is small, and the anti-reflective coating should then be chosen to reduce the reflectance of the electrolyte/
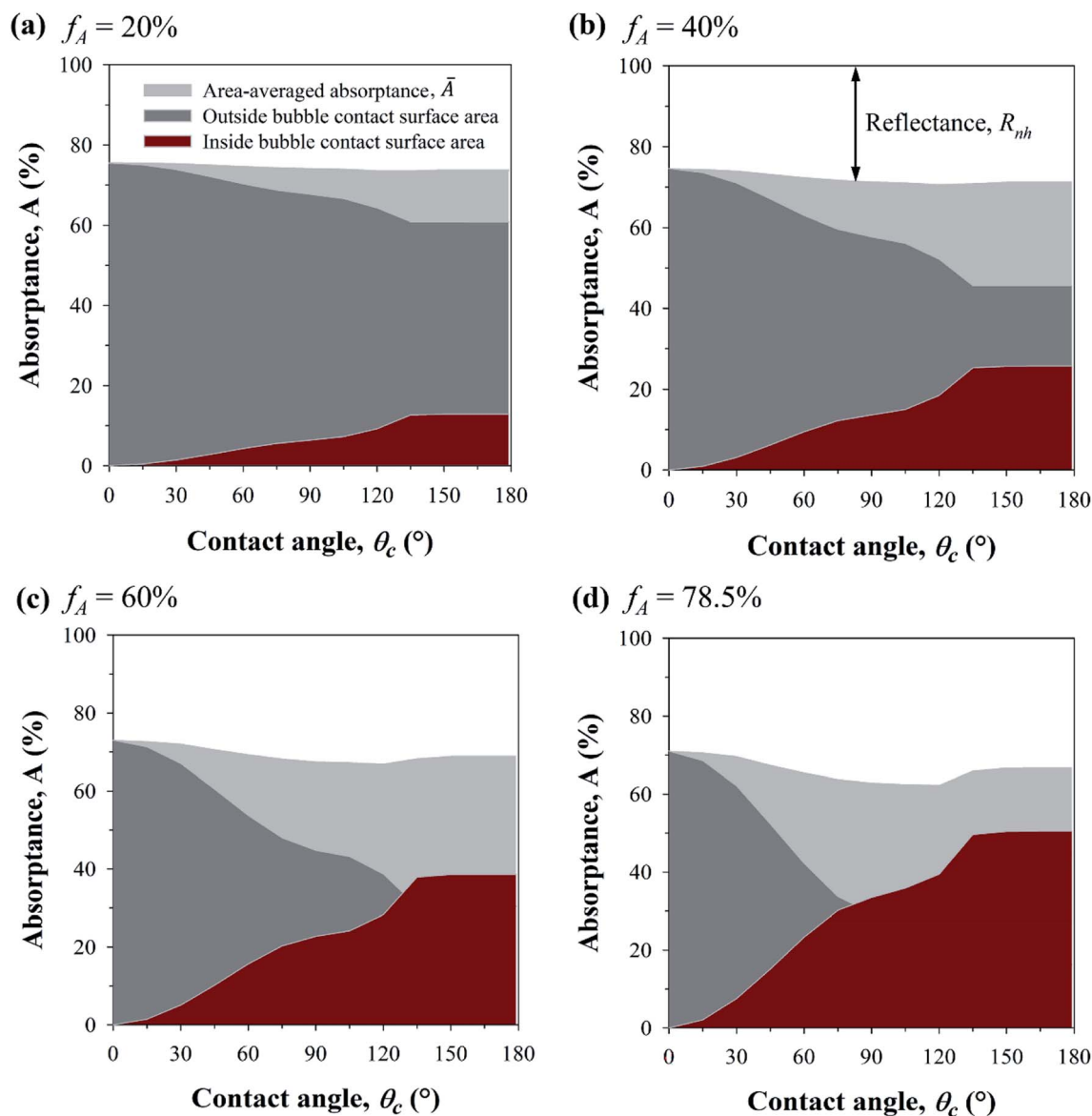
Fig. 10 Fractions of the incident radiation reflected and absorbed inside or outside the bubble contact surface area as functions of contact angle θ_c for projected surface area coverages (a) $f_A = 20\%$, (b) $f_A = 40\%$, (c) $f_A = 60\%$, and (d) $f_A = 78.5\%$.

photoelectrode interface only. For example, in the case of Si photoelectrodes considered in this study, a ~150 nm thick titania film could serve as an anti-reflective coating, as demonstrated experimentally in ref. 33 and 34. In fact, Seger et al.[34] reported an increase of around 15% in the saturation photocurrent density owing to the antireflective properties of titania. In addition, titania coatings exhibit photoinduced hydrophilicity[35] and also act as a protection layer for the photoelectrode.[20,33,34]

5. Conclusion

This paper presented a comprehensive study to assess and quantify the optical losses caused by the presence of non-absorbing cap-shaped gas bubbles on a large horizontal Si photoelectrode immersed in an aqueous electrolyte. The Monte

Carlo ray-tracing method was utilized to predict (i) the normal hemispherical reflectance R_{nh}, (ii) the area-averaged absorptance $\bar{A}$, and (iii) the local variations in the absorbed photon flux $A(x,y)$. The normal hemispherical reflectance of a photoelectrode without bubbles was used as a reference. It was established that bubble diameter and polydispersity did not have any significant effect on the optical losses for a given projected surface area coverage f_A. However, the optical losses depended on the contact angle and increased with f_A. Three different optical regimes were defined to explain the variation of optical losses with bubble contact angle θ_c based on the interplay of total internal reflection at the electrolyte/bubble interface and reflection at the bubble/photoelectrode interface. Overall, a maximum of 18% loss in the area-averaged absorptance was predicted in the photoelectrode covered with bubbles of contact angle $\theta_c = 120°$ and projected area coverage $f_A =$

78.5%. Scattering by bubbles also caused substantial local variation in the absorbed photon flux, with significant light concentration up to a factor 2 outside the projected footprint of the bubble compared to a bare photoelectrode. The magnitude of absorbed photon flux just outside the bubble projected footprint was up to 4 times that inside. It was established that photoelectrodes with hydrophilic materials or coatings should be preferred to minimize the optical losses caused by the presence of bubbles. However, in these conditions, the bubbles significantly redistributed the incident radiation on the photo-electrode surface, which may lead to more optical losses when performing experiments with small (mm-scale) photoelectrodes due to losses from the edges. In addition, an anti-reflective coating aimed at minimizing the reflectance of the electrolyte/photoelectrode interface can further reduce the back-scattering losses from the photoelectrode. However, at high bubble coverages and high contact angles, it would be beneficial to use an anti-reflective coating that minimizes the reflectance of the bubble/photoelectrode interface instead. Finally, high bubble coverages not only increase the optical losses but also the kinetic and ohmic losses. Therefore, convection in the electrolyte and/or the use of surfactants can facilitate the removal of bubbles.

Author contributions

Abhinav Bhanawat: conceptualization, methodology, validation, formal analysis, investigation, visualization, writing – original draft, writing – reviewing and editing. Keyong Zhu: software, formal analysis. Laurent Pilon: supervision, conceptualization, writing – reviewing and editing, funding acquisition.

Conflicts of interest

There are no conflicts of interest to declare.

Abbreviation

A	Absorptance
$\bar{A}$	Area-averaged absorptance
$A(x,y)$	Local absorptance in a bin at location (x,y)
c	Speed of light in vacuum (m s^{-1})
CL	Centerline of the bubble
D	Bubble diameter (mm)
d_c	Diameter of the contact circle (mm)
d_p	Projected diameter of bubble (mm)
d_t	Diameter of the circle outside which total internal reflection occurs (mm)
EQE	External quantum efficiency
f_A	Projected surface area coverage (%)
f_S	Contact surface area coverage (%)
h	Planck's constant (m^2 kg s^{-1})
H	Thickness of the photoelectrode (mm)
I	Incident intensity (W m^{-2} s)
IQE	Internal quantum efficiency

$\bar{J}_{ph}$	Area-averaged photocurrent density of a photoelectrode (A m^{-2})
k	Absorption index
L	Length of the square photoelectrode (mm)
M	Total number of bins in each axis
n	Refractive index
N_i	Number of incident photons on the photoelectrode
N_a	Number of absorbed photons in the photoelectrode
$N_a(x,y)$	Number of absorbed photons in a bin at location (x,y)
q	Charge of an electron (C)
R	Reflectance
r_c	Radius of the contact circle (mm)
r_p	Projected radius of the circle (mm)
r_t	Radius of the circle outside which total internal reflection occurs (mm)

Greek symbols

λ	Wavelength of the incident radiation (nm)
ρ	Interface reflectance
θ_c	Contact angle (°)
θ_{cr}	Critical contact angle (°)

Subscripts

0	Bare photoelectrode
b	Bubble
e	Electrolyte
p	Photoelectrode
nh	Normal-hemispherical

Acknowledgements

References

1 J. Li and N. Wu, Semiconductor-based photocatalysts and photoelectrochemical cells for solar fuel generation: a review, *Catal. Sci. Technol.*, 2015, **5**(3), 1360–1384.
2 N. S. Lewis, Research opportunities to advance solar energy utilization, *Science*, 2016, **351**, 6271.
3 J. Barber, Hydrogen derived from water as a sustainable solar fuel: learning from biology, *Sustainable Energy Fuels*, 2018, **2**(5), 927–935.
4 J. H. Kim, D. Hansora, P. Sharma, J.-W. Jang and J. S. Lee, Toward practical solar hydrogen production – an artificial

photosynthetic leaf-to-farm challenge, *Chem. Soc. Rev.*, 2019, **48**(7), 1908–1971.

5 H. Wu, *et al.*, Photocatalytic and photoelectrochemical systems: similarities and differences, *Adv. Mater.*, 2020, **32**(18), 1904717.

6 T. H. Jeon, M. S. Koo, H. Kim and W. Choi, Dual-functional photocatalytic and photoelectrocatalytic systems for energy- and resource-recovering water treatment, *ACS Catal.*, 2018, **8**(12), 11542–11563.

7 B. D. James, G. N. Baum, J. Perez and K. N. Baum, *Technoeconomic analysis of photoelectrochemical (PEC) hydrogen production, DOE report*, 2009.

8 Z. Chen, *et al.*, Accelerating materials development for photoelectrochemical hydrogen production: standards for methods, definitions, and reporting protocols, *J. Mater. Res.*, 2010, **25**(1), 3–16.

9 M. T. Spitler, *et al.*, Practical challenges in the development of photoelectrochemical solar fuels production, *Sustainable Energy Fuels*, 2020, **4**(3), 985–995.

10 A. Angulo, P. van der Linde, H. Gardeniers, M. Modestino and D. F. Rivas, Influence of bubbles on the energy conversion efficiency of electrochemical reactors, *Joule*, 2020, **4**(3), 555–579.

11 A. E. Dorfi, A. C. West and D. V. Esposito, Quantifying losses in photoelectrode performance due to single hydrogen bubbles, *J. Phys. Chem. C*, 2017, **121**(48), 26587–26597.

12 F. Njoka, S. Mori, S. Ookawara and M. Ahmed, Effects of photo-generated gas bubbles on the performance of tandem photoelectrochemical reactors for hydrogen production, *Int. J. Hydrogen Energy*, 2019, **44**(21), 10286–10300.

13 P. J. Sides and C. W. Tobias, Resistance of a planar array of spheres: gas bubbles on an electrode, *J. Electrochem. Soc.*, 1982, **129**(12), 2715.

14 H. Vogt, The incremental ohmic resistance caused by bubbles adhering to an electrode, *J. Appl. Electrochem.*, 1983, **13**(1), 87–88.

15 L. Janssen and S. Van Stralen, Bubble behaviour on and mass transfer to an oxygen-evolving transparent nickel electrode in alkaline solution, *Electrochim. Acta*, 1981, **26**(8), 1011–1022.

16 K. Obata and F. Abdi, Bubble-Induced Convection Stabilizes Local pH during Solar Water Splitting in Neutral pH Electrolytes, *Sustainable Energy Fuels*, 2021, **5**(15), 3791–3801.

17 C. Xiang, *et al.*, Modeling, simulation, and implementation of solar-driven water-splitting devices, *Angew. Chem., Int. Ed.*, 2016, **55**(42), 12974–12988.

18 M. A. Modestino, S. M. H. Hashemi and S. Haussener, Mass transport aspects of electrochemical solar-hydrogen generation, *Energy Environ. Sci.*, 2016, **9**(5), 1533–1551.

19 I. Holmes-Gentle, F. Bedoya-Lora, F. Alhersh and K. Hellgardt, Optical losses at gas evolving photoelectrodes: implications for photoelectrochemical water splitting, *J. Phys. Chem. C*, 2018, **123**(1), 17–28.

20 P. A. Kempler, Z. P. Ifkovits, W. Yu, A. I. Carim and N. S. Lewis, Optical and electrochemical effects of H_2 and O_2 bubbles at upward-facing Si photoelectrodes, *Energy Environ. Sci.*, 2021, **14**(1), 414–423.

21 G. Nagayama, S.-I. Shi-Iki and T. Tsuruta, Effects of nanostructures on surface wettability: a molecular dynamics study, *Nippon Kikai Gakkai Ronbunshu, B-hen*, 2007, **19**(4), 1084–1091.

22 K. Hashimoto, H. Irie and A. Fujishima, TiO_2 photocatalysis: a historical overview and future prospects, *Jpn. J. Appl. Phys.*, 2005, **44**(12), 8269.

23 S. Lubetkin, Thermal Marangoni effects on gas bubbles are generally accompanied by solutal Marangoni effects, *Langmuir*, 2003, **19**(26), 10774–10778.

24 M. F. Modest, *Radiative Heat Transfer*, Academic Press, New York, NY, 2013.

25 J. R. Howell, M. P. Mengüç, K. Daun and R. Siegel, *Thermal Radiation Heat Transfer*, CRC Press, Boca Raton, FL, 7th edn, 2020.

26 K. Zhu, Y. Huang, J. Pruvost, J. Legrand and L. Pilon, Transmittance of transparent windows with non-absorbing cap-shaped droplets condensed on their backside, *J. Quant. Spectrosc. Radiat. Transfer*, 2017, **194**, 98–107.

27 K. Zhu and L. Pilon, Transmittance of semitransparent windows with absorbing cap-shaped droplets condensed on their backside, *J. Quant. Spectrosc. Radiat. Transfer*, 2017, **201**, 53–63.

28 M. A. Green, Self-consistent optical parameters of intrinsic silicon at 300 K including temperature coefficients, *Sol. Energy Mater. Sol. Cells*, 2008, **92**(11), 1305–1310.

29 H. Berberoglu, J. Yin and L. Pilon, Light transfer in bubble sparged photobioreactors for H_2 production and CO_2 mitigation, *Int. J. Hydrogen Energy*, 2007, **32**(13), 2273–2285.

30 A. Vilanova, T. Lopes, C. Spenke, M. Wullenkord and A. Mendes, Optimized photoelectrochemical tandem cell for solar water splitting, *Energy Storage Materials*, 2018, **13**, 175–188.

31 O. Khaselev and J. A. Turner, A monolithic photovoltaic-photoelectrochemical device for hydrogen production via water splitting, *Science*, 1998, **280**(5362), 425–427.

32 S. S. Kocha, D. Montgomery, M. W. Peterson and J. A. Turner, Photoelectrochemical decomposition of water utilizing monolithic tandem cells, *Sol. Energy Mater. Sol. Cells*, 1998, **52**(3–4), 389–397.

33 W.-H. Cheng, *et al.*, Monolithic photoelectrochemical device for direct water splitting with 19% efficiency, *ACS Energy Lett.*, 2018, **3**(8), 1795–1800.

34 B. Seger, T. Pedersen, A. B. Laursen, P. C. Vesborg, O. Hansen and I. Chorkendorff, Using TiO_2 as a conductive protective layer for photocathodic H_2 evolution, *J. Am. Chem. Soc.*, 2013, **135**(3), 1057–1064.

35 X. Hu, Z. Cao, Y. Wang, S. Shen, L. Guo and J. Chen, Single photogenerated bubble at gas-evolving TiO_2 nanorod-array electrode, *Electrochim. Acta*, 2016, **202**, 175–185.